

MASS OF CLUSTERS IN SIMULATIONS

ANDREA V. MACCIÒ^{1,2}, GIUSEPPE MURANTE³ & SILVIO A. BONOMETTO^{1,2}

Draft version July 24, 2021

ABSTRACT

We show that dark matter halos, in n-body simulations, have a *boundary layer* (BL), which neatly separates dynamically bound mass from unbound materials. We define $T(r)$ and $W(r)$ as the differential kinetic and potential energy of halos and evaluate them in spherical shells. We notice that, in simulated halos, such differential quantities fulfill the following properties: (i) The differential virial ratio $\mathcal{R} = -2T/W$ has at least one *persistent* (resolution independent) minimum \bar{r} , such that, close to \bar{r} , (ii) the function $w = -d \log W / d \log r$ has a maximum, while (iii) the relation $\mathcal{R}(\bar{r}) \simeq w(\bar{r})$ holds. BL's are set where these three properties are fulfilled, in halos found in simulations of TCDM and Λ CDM models, run *ad-hoc*, using the ART and GADGET codes; their presence is confirmed in larger simulations of the same models, with a lower level of resolution. Here we find that $\sim 97\%$ of the ~ 300 clusters (per model) we have with $M > 4.2 \cdot 10^{14} h^{-1} M_{\odot}$, owns a BL. Those clusters which appear not to have a BL are seen to be undergoing major merging processes and to grossly violate spherical symmetry. The radius $\bar{r} \equiv r_c$ has significant properties. First of all, the mass M_c it encloses almost coincides with the mass M_{dyn} , evaluated from the velocities of all particles within r_c , according to the virial theorem. Also, materials at $r > r_c$ are shown not be in virial equilibrium. Using r_c we can then determine an individual density contrast Δ_c for each virialized halo, that we compare with the "virial" density contrast $\Delta_v \simeq 178 \Omega_m^{0.45}$ (where Ω_m is the matter density parameter) obtained assuming a spherically symmetric and unperturbed fluctuation growth. As expected, for each mass scale, Δ_v is within the range of Δ_c 's. However the spread in Δ_c is wide, while the average Δ_c is $\sim 25\%$ smaller than the corresponding Δ_v . We argue that the matching of properties derived under the assumption of spherical symmetry must be a consequence of an approximate sphericity, after violent relaxation destroyed features related to ellipsoidal non-linear growth. On the contrary, the spread of final Δ_c is an imprint of the different initial 3-D geometries of fluctuations and of the variable environment during their collapse, as suggested by a comparison of our results with Sheth & Tormen analysis.

Subject headings: galaxies: clusters: general — cosmology: theory — dark matter — large-scale structure of the Universe — methods: N-body simulations

1. INTRODUCTION

The inner region of dark matter halos in n-body simulations is certainly virialized. A precise detection of the boundaries of such a region, however, is a long-lasting and not yet completely solved problem. If we try just to identify a "collapsed" region, *i.e.* a region detached from the cosmological expansion, the task is easier (see, e.g., Monaco & Murante 1999 and references therein). However, in general, a collapsed region is not yet in virial equilibrium. The point is that, in a cosmological context, each structure is embedded in a more or less homogeneous background, and we pass gradually from the inner halo to external materials. The aim of this work is to show a precise criterion able to find virialized regions in dark matter halos. This criterion will be tested on simulations and found to be more efficient than previously adopted rules.

As a matter of fact, several global properties of galaxy clusters, such as mass (M), radius (r) and, also, temperature (T_X) or luminosity (L_X) are strictly linked to the achievement of equilibrium. Analytical predictions on such global quantities were performed assuming that structures evolve from uniform, spherically symmetric fluctuations,

preserve such symmetries during their growth and feel no influence from their environment (Gott & Rees 1975, Peebles 1980). However, even under such simplifying conditions, a cosmological constant is a significant complication. Lahav et al (1991) studied the growth of uniform spherical fluctuations within such context. They also outlined that the most direct way through which observations can distinguish among flat models with different Ω_m (matter density parameter) is comparing cluster abundances at low and high redshift. The dynamics of the spherically symmetric growth of a uniform density fluctuation, in a model with $\Omega_m + \Omega_{\Lambda} = 1$ (where Ω_{Λ} is the vacuum density parameter), was further explored by Eke et al (1996). Brian and Norman (1998) gave a polynomial expression for the expected density contrast of virialized clusters, which reads $\Delta_v = A + Bx + Cx^2$, with $x = \Omega_m - 1$, and $A = 18\pi^2 \simeq 178$, $B = 82$, $C = -39$, and holds at any redshift z ; this relation is well approximated by the expression:

$$\Delta_v = A\Omega_m^{0.45} . \quad (1.1)$$

Under the same assumptions, using a Press & Schechter (1974) approximation, one can predict the expected mass function of clusters.

¹Department of Physics G. Occhialini, Università di Milano-Bicocca, Piazza della Scienza 3, I 20126 Milano (Italy)

²I.N.F.N., Via Celoria 16, I20133 Milano (Italy)

³I.N.A.F., Osservatorio Astronomico di Torino – Torino (Italy)

The impact of this approximation on the estimate of cluster global quantities could be appreciated only through numerical simulations. Much work was therefore devoted to this aim (see, e.g., Lacey & Cole, 1993,1994; Cole & Lacey 1996; Carlberg et al., 1996; Eke et al. 1996; Eke et al. 1998; Brian & Norman, 1998; Gardini et al. 1999). However, in the very analysis of the numerical work, the above approximations were often implicit. An example is the identification of dark halos based on spherical overdensity (SO) algorithms, with reference to the density contrast Δ_v given in eq. (1.1). In this work we shall also use an SO algorithm (described below) as a selection criterion. However, using eq. (1.1), to work out values for the cluster radius (r_v) or mass (M_v), implies a bias. The values (1.1) are obtained under precise restrictions and numerical work should also verify their impact. In a sense, the problem is even more severe when the values (1.1) are used to define virialized halos without requiring explicitly that they are spherical.

In this work we plan to find a rule, suitable for defining virialized systems, taking into account that a variety of growth histories led to different final features of virialized structures. A number of recent papers (Sheth & Tormen (1999, 2002), Sheth, Mo & Tormen, 2001) had a similar motivation. They tried to study the growth of primeval fluctuations taking into account the effect of an ellipsoidal collapse. Then, in order to avoid having the collapse on some axis going to zero, they set up a recipe to freeze it out once it has shrunk by some critical factor. This freeze-out radius is explicitly chosen so that the density contrast at virialization for the whole halo is again Δ_v as given in eq. (1.1), *i.e.* in spherical growth models. In contrast, in this work the use of Δ_v to define virialized systems is completely overcome. The point is that the detailed growth history of individual halos, in which different ellipticities and velocity anisotropies played an important role, is not expected to leave major traces on final halo shapes after violent relaxation has occurred during the virialization process (Navarro, Frenk & White 1997). On the other hand, it may result in a significant spread of the equilibrium density contrasts Δ_c of individual halos. Therefore, when the virial radius of relaxed objects is sought, deviations from spherical symmetry and velocity anisotropies may not be as important as deviations of Δ_c from Δ_v .

We expect that the value Δ_v , given by eq. (1.1), is within the range of the actual Δ_c values, but we think that it is important to first test how extended this range is, and how Δ_v is set with respect to actual values. Furthermore, a different Δ_c implies a different radius and mass (r_c and M_c) for each object. Accordingly, we expect that some individual object masses increase and others decrease. We will explore the extent of these changes on galaxy clusters in numerical simulations of critical CDM models with and without a cosmological constant. Such changes may have an impact on the mass function (see section 5 and Fig. 13 and 14), while some scaling relations might be significantly altered, for instance the relation between M and T_X .

In order to implement our program, we need a simple and effective rule to identify virialized material in clusters. In trying to find such rule we discovered a precise regularity in the transition region between material belonging to clusters and the surrounding medium. In fact, the volume occupied by virialized materials is confined by

a *boundary layer* (BL), whose depth Δr ranges around 50–100 h^{-1} kpc, and whose properties fulfill precise analytical prescriptions. Such a BL has been found in $\sim 97\%$ of the clusters in our simulated models and is one of the findings of this work.

The BL is not a physical confinement barrier, and particles can travel outwards and inwards through it. On the contrary, it confines a volume, where material fulfills precise equilibrium conditions, which cease to hold outside it. Inside the BL itself, the formal condition for virial equilibrium of an isolated system holds, as pressure forces at its upper and lower borders cancel each other; on the BL, kinetic energy has a minimum with respect to potential energy, and matter density is rapidly decreasing. These conditions follow from a precise analytical requirement (Rw requirement) derived under the assumption of spherical symmetry. This Rw requirement will be only approximately satisfied by halos in simulations, where the halo geometries apparently violate spherical symmetry. We show, however, that normal deviations from a spherical shape in DM halos do not prevent them from having a BL.

We explicitly note that we do not *force* the BL to exist, but we apply the Rw requirement and *find* it. For this reason, finding the BL is different from finding a given spherical overdensity; the latter always exists when average densities of halos decrease with increasing radii, and this does not imply even an approximately spherical symmetry. On the contrary, we could have bound and relaxed regions which are not confined by a BL: our analysis of numerical simulations shows that this is not the case. There is also a major difference between the Rw requirement we are defining here, and other prescriptions, such as SKID, which defines a halo as the set of all particles *gravitationally bound* to the halo itself. In fact, bound particles are not guaranteed to belong to virialized zones and may belong to regions which are bound but still unrelaxed.

In this paper we shall first discuss when the BL should exist and introduce the Rw requirement used to detect it. To have significant statistics based on this rule and to confirm its validity requires simulations performed with a large dynamic range, as can only be done by parallel computing.

Finding and situating BL's allows a better evaluation of individual cluster masses, radii and density contrasts, as well as an analysis of their possible dependence on various physical parameters. The study of the structure of dark matter halos in numerical simulations can also be put on a sounder footing. In previous analyses (see, e.g., Cole & Lacey 1996) the r dependence of the integral virial ratio $-2T(<r)/W(<r)$ was discussed and found not to be “useful for defining the boundaries of the virialized region”. One of the findings of our analysis is precisely the possibility of detecting such a boundary, using the virial ratio for shells instead of spheres. Fig. 1 compares integral and differential virial ratios, showing how much more information appears to be contained in the latter (see Sec. 3 for details on how $\mathcal{R}(r)$ points are calculated). Previous analyses have also stressed halo properties apparently depending “on how groups are identified” (Sheth et al., 2001). The existence of a border, with precise physical properties, excluding cluster material lets one overcome any such ambiguity.

It may be also important to remember that according

to the definitions given above, in this work Δ_v , r_v , M_v are quantities worked out starting from the fixed density contrast given by (1.1), while Δ_c , r_c , M_c are the same quantities when worked out from the setting of the BL around each cluster. Let us also point out that CHb the procedure discussed in this work is not the basis for an CHe alternative cluster-finding algorithm, such as, e.g., Friends-of-Friends, SKID or SO. On the contrary, our analysis assumes that cluster locations are given. Here we give a different prescription for defining the physical dimension of the cluster, not its position.

The plan of the paper is as follows. In section 2 we give suitable information on the simulations used, which were partially run *ad-hoc*, for this work. In section 3 and 4 we define the boundary layer (BL) and discuss how it can be found in simulated clusters. In section 5 we show the results of our work, and in section 6 we discuss them and some future perspectives.

2. MODELS AND N-BODY SIMULATIONS

We use two main sets of simulations, performed with different codes: the parallel AP3M N-body code described in Gardini et al. (1999), the parallel PM ART code developed by Kratshov & Klypin (1997), and the parallel tree-code GADGET (Springel et al. 2001).

The code of Gardini et al. (1999) was developed from the serial public AP3M code of Couchman (1991), extending it to different cosmological models and allowing suitable flexibility in particle masses. Using this code, two simulations were performed. The first of them, dealing with a “tilted” Einstein-de Sitter model (hereafter TCDM), is the same already considered by Gardini et al. (1999); the normalization of the run was, however, rescaled to yield $\sigma_8 = 0.55$ at the final step, instead of $\sigma_8 = 0.61$, so that the final abundance of rich clusters is the same for both models at the final epoch (as usual, σ_8 is the m.s. density fluctuation on the scale of $8 h^{-1} \text{Mpc}$, h being the Hubble parameter in units of 100 km/s/Mpc). The latter simulation dealt with a Λ CDM model, i.e. a flat CDM universe with non-zero cosmological constant with $\sigma_8 = 1.08$. Owing to recent observational results (see, e.g., Schuecker et al. 2002), these normalizations are both rather high, as a reasonable value for σ_8 in Λ CDM models is ~ 0.75 ; however, this has no impact when studying inner cluster dynamical properties.

The above simulations (denoted A and B, respectively) are performed in cubes with sides of $360 h^{-1} \text{Mpc}$. CDM+baryons are represented by 180^3 particles, whose individual mass is $2.22 \cdot 10^{12} h^{-1} M_\odot$ for TCDM and $0.777 \cdot 10^{12} h^{-1} M_\odot$ for Λ CDM. We use a 256^3 grid to compute the FFT’s needed to evaluate the long range contribution to the force (PM) and we allow for mesh refinement where the particle density attains or exceeds ~ 30 times the mean value. The starting redshifts are $z_{in} = 10$ for TCDM and $z_{in} = 20$ for Λ CDM. The particle sampling of the density field is obtained by applying the Zel’dovich approximation (Zel’dovich 1970; Doroshkevich et al. 1980) starting from a regular grid. We adopt the same random phases in both A and B.

The number of steps were 1000 equal p -time steps (the time parameter is $p \propto a^{2/3}$, where a is the expansion factor). The comoving force resolution, given by the softening

length, is $\eta \simeq 112 h^{-1} \text{kpc}$, yielding a Plummer equivalent softening $\epsilon_{pl} \simeq 40.6 h^{-1} \text{kpc}$. These simulations were described in more detail in Gardini et al. (1999), and were also used in Macciò et al. (2002). The parameters of the models are reported in detail in Table 1.

In order to see how resolution affects the results of the Rw requirement, we performed further simulations with the ART code (courtesy of A. Klypin). This allows us to select regions inhabited by clusters and to re-run them with increasing particle mass resolution: from $7.7 \times 10^{11} \Omega_m h^{-1} M_\odot$ to $1.2 \times 10^{10} \Omega_m h^{-1} M_\odot$.

The ART code (Adaptive Refinement Tree: Kravtsov et al. 1997, Knebe et al. 2000) starts with a uniform grid, which covers the whole computational box. This grid defines the lowest (zeroth) level of resolution of the simulation. The standard Particles-Mesh algorithms are used to compute the density and gravitational potential on the zeroth-level mesh. The code then reaches high force resolution by refining all high density regions using an automated refinement algorithm. The refinements are recursive: the refined regions can also be refined, each subsequent refinement having half of the previous level’s cell size. This creates a hierarchy of refinement meshes of different resolution, size, and geometry covering regions of interest. Because each individual cubic cell can be refined, the shape of the refinement mesh can be arbitrary and effectively match the geometry of the region of interest. This algorithm is well suited for simulations of a selected region within a large computational box.

The criterion for refinement is the local density of particles: if the number of particles in a mesh cell (as estimated by the Cloud-In-Cell method) exceeds the level n_{thresh} , the cell is split (“refined”) into 8 cells of the next refinement level. The refinement threshold may depend on the refinement level. The code uses the expansion parameter a as the time variable. Besides spatial refinements, during the integration time refinements are also performed.

The ART code can handle particles of different masses. This lets us increase the mass (and correspondingly the force) resolution of regions centered around the highest mass clusters. The multiple mass resolution is implemented in the following way. We first set up a realization of the initial spectrum of perturbations, so that initial conditions for our largest number (512^3) of particles can be generated in the simulation box. Coordinates and velocities of all the particles are then calculated using all waves ranging from the fundamental mode $k = 2\pi/L$ to the Nyquist frequency $k = 2\pi/L \times N^{1/3}/2$, where L is the box size and N is the number of particles in the simulation. We obtained lower resolution regions by merging high resolution particles into particles of larger mass where needed. This process can be repeated to get still lower resolution. The larger mass (merged) particles have velocities and displacements equal to the average of the velocities and displacements of the smaller-mass particles. Using this technique we firstly generated initial conditions for low-resolution simulations. These simulations were run from their initial redshift to $z = 0$ and they were used to locate the Lagrangian regions forming the most massive clusters. Then, we were able to obtain initial conditions at high resolution (both in force and mass) in the selected Lagrangian zones, with the same random Fourier phases.

Such zones were surrounded by lower and lower resolution shells taking into account the tidal field which acts on them. Finally, these ICs were used to run the high-resolution cluster simulations.

The simulations employed here were performed using 128^3 zeroth-level grid in a computational box of $180h^{-1}\text{Mpc}$. The threshold for cell refinement (see above) was low on the zeroth level: $n_{\text{thresh}}(0) = 2$. Thus, every zeroth-level cell containing two or more particles was refined. The threshold was higher on deeper levels of refinement: $n_{\text{thresh}} = 3$ and $n_{\text{thresh}} = 4$ for the first level and higher levels, respectively.

For the low resolution runs the step in the expansion parameter was chosen to be $\Delta a_0 = 2 \times 10^{-3}$ on the zeroth level of resolution. This gives about 500 steps for particles located in the zeroth level for an entire run to $z = 0$ and 128.000 for particles at the highest level of resolution.

Using the ART code we performed two simulations: a ΛCDM model and a TCDM model, that we will indicate as C and D, respectively. These models are similar, although not identical, to those of Gardini et al. 1999; their parameters are listed in Table 2. We identified the clusters in these zero-level simulations and selected the 6 largest mass clusters for each cosmological model. They were re-run with increased mass (and force) resolution, using the method described above. For every selected cluster we have three runs with resolutions ⁴ of 128^3 (particles mass $M_p = 7.7 \times 10^{11} \Omega_m h^{-1} M_\odot$), 256^3 ($M_p = 9.6 \times 10^{10} \Omega_m h^{-1} M_\odot$) and 512^3 ($M_p = 1.2 \times 10^{10} \Omega_m h^{-1} M_\odot$) with more than 350.000 particles within a radius of $2.0 \text{ Mpc } h^{-1}$.

We then run 3 out of the 6 high resolution ΛCDM clusters with the public parallel tree-code GADGET (Springel et al. 2001), to verify that our results do not depend upon the peculiarities of one N-body code. One of the clusters was magnified with both ART and GADGET. The initial conditions were set as described above. We used a Plummer-equivalent softening length $\epsilon = 10.98$; this is also the linear dimension of our highest-resolution ART cell. We chose the time-step criterion 3, based on the local dynamical time, with a tolerance of the integration error $E_{\text{int}} = 0.2$, which gave us more than 100000 time steps from z_{in} to $z = 0$. The criterion for opening the tree-cells is based on the absolute truncation error in the multipole expansion, with a tolerance on the error on the force of $E_F = 0.02$ (see Springel et al. 2001 and the code user manual for more details).

In all of our numerical simulations, clusters were identified using a SO algorithm. As a first step, candidate clusters are located by a FoF algorithm, with linking length $\lambda = \phi \times d$ (here d is the average particle separation), keeping groups with more than N_f particles. We then perform two operations: (i) we find the point, C_W , where the gravitational potential, due to the group of particle, is minimum; (ii) we determine the radius, \bar{r} , of a sphere centered in C_W where the density contrast is Δ_v . Using all particles in this sphere we perform again the operations (i) and (ii). The procedure is iterated until we converge onto a stable particle set. The set is discarded if, at some stage, we have less than N_f particles. If a particle is a potential member of two groups it is assigned to the more massive one. (Gardini et al. 1999 also describe this SO algorithm

in more detail and compare it with other group identification algorithms, e.g. Governato et al. 1999). In this work we set $\phi = 0.2$ and take N_f so to have a mass threshold $3.0 \times 10^{13} h^{-1} M_\odot$. Above this mass threshold there are ~ 10000 halos in the simulations A,B and ~ 1250 halos in the simulations C,D.

Tests performed by Gardini et al. (1999) show that no cluster is missed above $4.2 \times 10^{14} h^{-1} M_\odot$. We have 303 such clusters in A, 316 in B, 40 in C, 36 in D; 6 clusters of C and D where then blown up to various resolution levels.

3. THE VIRIAL THEOREM APPLIED TO SINGLE CLUSTERS: THEORY

Finding the volume where cluster materials are in virial equilibrium may seem a tough and somewhat ambiguous task. If kinetic and potential energies, within a radius r , are defined according to:

$$2T(< r) = \sum_i (r_i < r) m v_i^2, \quad (3.1)$$

$$W(< r) = - \sum_{i < j} (r_{i,j} < r) \frac{G m^2}{r_{ij}}, \quad (3.2)$$

the virial ratio

$$\mathcal{R}(< r) = - \frac{2T(< r)}{W(< r)} \quad (3.3)$$

should be unity, in a virialized sphere of radius r , provided that it is fully isolated. On the contrary, in the real world, as well as in simulations, the virialized volume is bordered by infalling and outgoing material, possibly traveling through a partially depleted area. For this reason, the convergence of $\mathcal{R}(< r)$ to unity, at a precise radius r , should not even be expected.

In principle, one can take into account such perturbations by fixing a radius r well inside the cluster volume and adding a *pressure term* to take into account external material, as has been done in observational work aiming to estimate the mass of optical clusters (see, e.g., Girardi et al., 1998). Accordingly, the virial equilibrium condition reads

$$2T + W = 3Vp \quad (3.4)$$

(V is the volume occupied by virialized material and p is the pressure at its borders). Eq. (3.4) translates the problem into finding a reasonable estimate for p .

The problem can also be considered from a slightly different point of view: if we find, around the cluster, a *boundary layer* (BL), which is in virial equilibrium by itself, and above which virial equilibrium is lost, its very material and all material it borders, down to the cluster center, need to be in stationary equilibrium. Particles may pass through this BL in both directions, but the overall virial balance shall keep constant in time.

We will now assume that this BL is spherical. The conditions found under this restriction are, however, well approximated by simulated halos. This seems to indicate that, even after a strongly asymmetric growth, the final

⁴Since our averaging procedure corresponds to using different mesh sizes when generating ICs for a simulation, we will refer to the size of the higher resolution mesh used in each simulation IC when quoting resolutions.

virialization process tends to partially suppress elliptical features.

The r dependence of the potential energy can be derived by performing the sums in eq. (3.2) starting with the outside:

$$\begin{aligned} W(< r) &= -\sum_i (r_i < r) \sum_j (r_j < r_i) \frac{Gm^2}{r_{ij}} = \\ &= -\sum_i (r_i < r) \mathcal{Z}(r_i), \end{aligned} \quad (3.5)$$

where the last term is the very definition of \mathcal{Z} . In the continuous limit (and still assuming spherical symmetry)

$$\mathcal{Z}(r) = Gm \int_0^r d^3r' \frac{\rho(r')}{|r-r'|} \quad (3.6)$$

with a suitable density, ρ . Quite in general, a volume integral of $\rho(r)$ increases with r . Henceforth,

$$\mathcal{Z}(r) = C(r/\bar{r})^{-w}, \quad (3.7)$$

where C is a normalization constant evaluated at an arbitrary position \bar{r} and $w (< 1)$ will, however, depend on r . Accordingly, it must be that

$$r \frac{d\mathcal{Z}}{dr}(r) = -[w + rw' \ln(\frac{r}{\bar{r}})] \mathcal{Z}(r). \quad (3.8)$$

Let us now suppose that there exists an interval $\Delta r = r_+ - r_-$, which satisfies the following conditions:

- (i) it is in virial equilibrium,
- (ii) the r dependence of pressure is such that the r.h.s. of eq. (3.4), yielding a term of the form $3(p_+ V_+ - p_- V_-)$, can be neglected in the virial balance,
- (iii) inside Δr , w is constant.

Further comments on the (ii) requirement can be found in Appendix A, where we show that halo profiles are expected to approach it. Together with (i), it implies that

$$\sum_i (r_i \in \Delta r) m v_i^2 - r_i \frac{d\mathcal{Z}}{dr}(r_i) = 0, \quad (3.9)$$

in the layer.

Let us then take into account the condition that w is constant and use eq. (3.8) with $w' = 0$ and the *virial ratio*

$$\mathcal{R}_{\Delta r} = \frac{\sum_i (r_i \in \Delta r) m v_i^2}{\sum_i (r_i \in \Delta r) \mathcal{Z}(r_i)}, \quad (3.10)$$

to obtain that

$$\mathcal{R} = w, \quad (3.11)$$

all along the interval Δr . This equation coincides with eq. (3.29) in Goldstein, Pole & Safko (2002) (in turn, the latter equation yields eq. (3.9) hereabove, in the limit $w \equiv \text{const.}$).

Requiring that $w' = 0$, then, also yields that

$$\frac{d\mathcal{R}}{dr} = 0, \quad (3.12)$$

in Δr . *Vice versa*, if the eqs. (3.11)–(3.12) are both fulfilled in a layer of depth Δr , this layer is at rest and in virial equilibrium. We thus define *boundary layer (BL)* a region of depth Δr satisfying eqs. (3.11)–(3.12).

Let us stress that the condition (iii) is essential to set the Rw requirement, defined by the eqs. (3.11)–(3.12). Unless w is constant along a suitable interval, we can neither replace $r_i d\mathcal{Z}(r_i)/dr$ by $-w\mathcal{Z}(r_i)$ in eq. (3.9), nor factorize w out of the sum, so to obtain eq. (3.11). Moreover, should eq. (3.11) hold on a single r , we could have $w' = 0$ there, with $\mathcal{R}' \neq 0$. Finding a layer fulfilling the Rw requirement, goes therefore beyond finding a layer in virial equilibrium. As we shall see, however, once the Rw requirement is fulfilled, we have found a layer bounding a virialized region.

Let us also stress that the Rw requirement does not imply that particles cannot pass through the BL; it only prescribes that such (possible) passages do not violate its stationary conditions. However, if we find about a cluster a boundary layer, it will act as a confinement barrier to inner kinetic and potential energies and mass. Notice that, in principle, inner materials might not be in virial equilibrium themselves; even in this case, however, there can be no net exchange of mass between inside and outside and the possible energy exchange is limited to the work done by tidal torques due to anisotropies.

Let us now show that no further material, outside the BL, can be in virial equilibrium. We will show that this is certainly forbidden if the values, taken by \mathcal{R} and w at r_+ , are a minimum and a maximum, respectively, when compared with values at $r > r_+$. This simple condition, however, is not strictly necessary; it is sufficient that the difference $\mathcal{R} - w$ increases, becoming positive, at $r > r_+$. This will be shown here below. Let us however anticipate that, while the Rw requirement can be fairly easily tested, it is not easy to deal with such further requirement. The tests performed on a large number of clusters and described in the next sections, however, let us conjecture that, when the Rw requirement is fulfilled, this further requirement is somehow inescapable. We now show why, at $r > r_+$, the equilibrium conditions are violated if a boundary layer is found. Notice that, at $r > r_+$, we can still assume that $W = W(r_+)(r/r_+)^{-w}$, but w , starting from the value it had in Δr , will now vary with r and, according to eq. (3.8),

$$\mathcal{R} - w = w' r \ln(r/r_+); \quad (3.13)$$

this equation cannot be fulfilled, if the difference $\mathcal{R} - w$, vanishing up to r_+ , increases at $r > r_+$, becoming positive. In fact we required that w is maximum and therefore $w' < 0$.

Let us finally notice that if a layer is characterized by higher w values, this means that it is emptier than inner or outer layers. A maximum of w , therefore, indicates a low density layer. In turn, a minimum of \mathcal{R} indicates a low kinetic energy, with respect to potential energy. BLs, therefore, are partially depleted r -intervals, where particles, on average, are particularly slow.

4. THE VIRIAL THEOREM APPLIED TO SINGLE CLUSTERS: PRACTICAL USE

The mathematical definition must now be applied to numerical simulations. A failure to find BLs could be attributed to insufficient numerical resolution or to bad violations of spherical symmetry. However, in principle, even if the resolution is enough and no substantial departures from sphericity are visible, BLs could still be absent.

Let us now describe our procedure. After finding clusters in simulations and their centers C_W , as described in sec. 2, we evaluated $W(r)$ and $\mathcal{R}(r)$, for spherical r -intervals containing a fixed number

$$N = M_4 / (2^4 m_p), \quad (4.1)$$

of particles (here M_4 of the total mass within $4.5 h^{-1} \text{Mpc}$ from C_W and m_p is the particle mass). However, successive points along r are obtained by shifting outwards by $N/8$ particles. In the relevant r range, the above criterion yields $N \sim 10^2$ for TCDM (simulation A) and $N \sim 3 \cdot 10^2$ for Λ CDM (simulation B), while successive points lay at a distance $\sim 20 h^{-1} \text{kpc}$. This is below (but not much below) the force resolution ($\sim 100 h^{-1} \text{kpc}$), as desired.

We do not expect BL's to be much thicker than our force resolution; accordingly, we first seek the minima of \mathcal{R} . Owing to the procedure by which \mathcal{R} points are worked out, a minimum is considered *significant* only if it is such with respect to 8 neighbors. Finding the maxima of w is harder, as $w(r)$, obtained by differentiating $W(r)$, should then be further differentiated to find its maxima. In practice, however, this second order differentiation is not needed. Quite in general, there will be just a few points r_m where \mathcal{R} has *significant* minima. Let then \mathcal{R}_m be the virial ratio at such points and let us fit $\tilde{W}(r)$ with the expression

$$\tilde{W} = A(r/r_m)^{-\mathcal{R}_m} \quad (4.2)$$

in $\nu = 8$ points $> r_m$, covering an interval $\Delta r \sim 100$ – $150 h^{-1} \text{kpc}$. The fit is performed in two steps: we first minimize the function $\phi = W/\tilde{W} - 1$ just using A as a parameter; then, in eq. (4.2), we allow \mathcal{R}_m to take values different from the value of \mathcal{R} in r_m , and perform a 2-parameter fit.

We considered the fit to be satisfactory, if two conditions hold: (i) When performing the first fit, the residual

$$\chi^2 = \sum_{i=1}^{\nu} \phi^2(r_i) < 10^{-3} \nu, \quad (4.2)$$

(i.e., a mean square discrepancy $\sim 3\%$, between the numerical values of $W(r)$ and its fitting expression, was our limit of tolerance). This detects r -intervals where eqs. (3.11)-(3.12) are both fulfilled. (ii) When performing the second fit, the best-fit value of \mathcal{R}_m is within $1-\sigma$ from the actual \mathcal{R}_m value. Here we test that also the slope of W is not too far from what is required. Such constraints should therefore select points where \mathcal{R} is minimum and (nearly) intersects w .

As outlined above, one might reasonably expect that a large fraction of clusters, at their boundaries, is far enough from sphericity that the expected system of maxima and minima, as well as their coincidences, is disrupted. The numerical noise in calculating w is also quite large and can be

expected to create severe problems. On the contrary, we found that *all clusters with mass $M > \sim 4.2 \cdot 10^{14} h^{-1} M_\odot$ have at least one value of r_m fulfilling the above requirements*, while some clusters have 2 or 3 points where the fitting criteria are fulfilled. In the few cases, when the fitting criteria were satisfied at more than one r_m , we discarded r_m values yielding Δ_c outside an interval $0.3 \Delta_v - 3 \Delta_v$. This selection criterion left us with $\sim 97\%$ of the initial clusters. When more than one r_m was still available, we selected the one corresponding to the smallest χ^2 ; this last criterion was needed for $\sim 10\%$ of the clusters only.

Let us recall again that the requirement of intersection between a minimum of \mathcal{R} and a maximum of w was found for spherical systems. When we deal with the halos of our simulations, sphericity is likely to be an approximation. When a single intersection exists, however, it is natural to guess that this is the point where the Rw requirement is best approached. However, both in this case and when several r_m points are found, it is natural to perform a closer inspection to make sure that no unexpected feature may bias our understanding of the physical situation.

This closer inspection requires an increased resolution. As described in sec. 2, a TCDM model and a Λ CDM model were then reconsidered within a smaller box with sides of $180 h^{-1} \text{Mpc}$, making use of the ART and GADGET codes. This gave us $\sim 1/8$ of the clusters provided by the AP3M simulations, but enabled us to focus on particular clusters, making use of the ART package facilities to increase the resolution there while still keeping identical boundary conditions. In order to test that the regularities found are not linked to peculiarities of the ART package, some clusters were magnified using GADGET, instead of ART. Altogether we have 12 clusters magnified, 6 for each model. 4 of the latter were obtained using ART and 3 using GADGET; hence, one cluster was magnified with both codes showing that our results are independent of the n -body code used. In fact, the final positions of particles have just minor differences, while \mathcal{R} and W coincide. A number of subsequent tests also concerned the stability of the minima of \mathcal{R} . In general, the number of local minima r_m decreases when the resolution is increased, but the point where W fits the expression (4.1) with the worst resolution is a minimum also with greater resolutions. In just a few cases, new minima arise when the resolution is improved; but in no case is a minimum yielding the BL erased when changing resolution. The “worst” cases for each model are shown in Fig. 2. Here we have a TCDM cluster, taken from the simulation C, which passes from 3 minima (128^3 particles), to 1 minimum (256^3 particles) and, again, to 3 minima (512^3 particles). The BL is displaced outwards by $\sim 150 h^{-1} \text{kpc}$, when we pass from 128 to 256; then, when passing from 256 to 512, no appreciable shift occurs. Out of the 12 clusters considered, only this one presents a shift slightly above the resolution of the initial simulation. The Λ CDM cluster of simulation D shown in Fig. 2, shows 4 minima with 128^3 particles, 2 minima with 256^3 particles and, again, to 3 minima with 512^3 particles; but when changing resolution, the shifts are $< 40 h^{-1} \text{kpc}$.

For these 12 clusters we follow in detail the joint behavior of \mathcal{R} and w . We show them in Fig. 3 for the best and worst cases we found. Of course, a precise coincidence between a minimum of \mathcal{R} and a maximum of w would indicate that, within the resolution limits, the system is spher-

ical. Seeking this kind of coincidence, therefore is somehow fatuous. Furthermore, in order to work out w , we ought to differentiate W , which is obtained from a discrete point distribution. Hence, although the nice coincidence of the *best* case is quite appealing, this case is not *safer* than the *worst* case we show. By tolerating a 3% disagreement in W , for $r/r_m < \sim 1.1$, we allow for a tolerance ~ 0.3 on the exponent w . In the worst case, we find a w - \mathcal{R} discrepancy of this order, but in most cases, $|w-\mathcal{R}|$ turns out to be ~ 0.1 . We tentatively conclude that this resolution is sufficient to show physical features and that the level of the w - \mathcal{R} (dis)agreement is a measure of the a -sphericity of actual systems. The important issue is that we *always* find a maximum of w to match the minimum of \mathcal{R} , quite close to the r_m selected at the initial resolution level.

This point can be further illustrated by Fig. 4, which shows a plot similar to Fig. 3, for a typical case at the initial resolution level. Both the \mathcal{R} and the w curves are much noisier here. \mathcal{R} , in particular, shows a wide set of local minima; the only *persistent* minima, however, are those marked by thick filled circles. As expected, the behavior of w is still noisier and most of the oscillations shown are clearly numerical. The role of w , however, just amounts to choosing among the points marked by a thick filled circle and selects the point marked by a vertical arrow. Even at this resolution level, the presence of a maximum of w , close to such point, can be suspected. When the resolution is increased, this maximum is more clearly visible, while no w maxima exist close to the other \mathcal{R} minima.

A further preliminary test of our technique, concerning galactic-sized and unvirialized DM halos, is given in Appendix B.

Before concluding this section, let us draw the reader's attention on the setting of the BL around particle agglomeration, as shown in Fig. 5 for a Λ CDM cluster. This figure shows that the BL is actually set outside of the main matter agglomeration; its spherical shape is somehow in contrast with the apparent a -sphericity of the cluster materials and easily justifies minor discrepancies from results based on an assumption of full spherical symmetry.

5. RESULTS

Once the sphere confining cluster materials is set, we can evaluate the density contrast Δ_c and the mass M_c inside it. In Figs. 6 and 7, points give Δ_c and M_c for all clusters in simulations A and B, respectively. They show a rather wide spread of Δ_c values. By subdividing the M_c abscissa in intervals of constant logarithmic width, we evaluate the average density contrast in each of them, to seek systematic trends with mass. Averages are still subject to a significant uncertainty owing to the spread of Δ_c . They are shown, at the 1 - σ level, in the plots. At high masses, some logarithmic intervals of Fig. 7 are empty or contain a single object. In the latter cases no error bar is given.

There seems to be no evidence of any peculiar trend of density contrasts with mass apart from, perhaps, a modest indication of an increasing density contrast at very high scales in Λ CDM. It is therefore possible to consider the overall average among Δ_c 's. This average is indicated by the continuous horizontal line and compared with the "virial" density contrast Δ_v , as given by eq. (1.1). In both cases, Δ_v (dotted line) is well inside the range of the den-

sity contrasts we found; the average Δ_c , however, in both cases, is smaller than Δ_v by $\sim 25\%$.

It is, however, clear that gravitationally evolved, stationary objects are *not* uniquely identified with a given, fixed density contrast. In further work, we plan to deal with the impact of variable Δ_c on the physical characteristics of DM halos, such as concentration, average angular momentum, density and velocity profiles. It may also be significant to test our results against the effects of different particle selection criteria, e.g. using the SKID algorithm instead of the SO one to pre-select the DM halos.

In Figs. 8 and 9 we plot r_c against M_c , for the simulations A and B, respectively. Here, error bars account for the variance of r_c around its average, which is wider than the error of the average r_c , shown in Fig. 6. Continuous and dotted curves show the expected behavior of r_c against M_c , when the density contrast is set either at the average Δ_c value or at Δ_v .

It is also significant to compare the plot of r_c against M_c with the behaviour of the radii r_c against the masses M_v of the corresponding clusters. This comparison is shown in Fig. 10, for the simulation A only; in order to avoid confusion, we omit error bars which, however, are approximately of the same size in both cases. The highest masses, for which error bars cannot be evaluated, are also omitted. Filled circles yield r_c vs. M_c , empty circles yield r_c vs. M_v . Filled circles nicely fit the line worked out from the average density contrast Δ_c ; only at high masses, where the statistics is poorer, some of the circles are far from this line. The same line is also a reasonable fit for the open circles. These, however, are systematically farther at all mass scales. In the figure, however, we also plot an horizontal line showing the average of the r_c values of all clusters with mass $> 4.2 \cdot 10^{14} h^{-1} M_\odot$. Even this average can be considered a reasonable fit for open circles (an unweighted χ^2 evaluation gives similar probabilities to both fitting lines). This plot shows that there are actual dangers, if quantities worked out assuming a constant Δ_v are compared with real data. In this case, one might tentatively suggest that there is a typical, mass independent, cluster radius $R \simeq 1.56 h^{-1} \text{Mpc}$, quite close to the Abell value. Our procedure, instead, outlines that this arises because some clusters were attributed a biased mass and the corresponding points were then set at a wrong abscissa. Although, altogether, this abscissa reshuffling is substantially casual, the danger that an characteristic scale erroneously appears is far from absent.

A critical result of our analysis is however shown in Figs. 11 and 12 (for simulations A and B, respectively). In simulations, the "numerical" cluster masses can be easily evaluated by summing up particle masses. The actual approach, in the real world, ought to be quite different and is based, first of all, on an analysis of galaxy velocities or X-ray emitting gas temperature. These analysis make use of the virial hypothesis; therefore, measured masses of galaxy clusters are estimates of their *dynamical* masses. It is therefore important to test how "numerical" cluster masses in simulations agree with the masses

$$M_{dyn} = \frac{\langle v^2 \rangle_{\{v,c\}} \cdot r_{\{v,c\}}}{G}, \quad (5.1)$$

evaluated averaging over the velocities of the particles within $r_{v,c}$. This comparison has been often performed,

showing a reasonable coincidence between M_v and M_{dyn} . The results of such fit are shown in Figs. 11 and 12 by the dashed histograms, which confirm the slight excess of M_{dyn} vs. M_v already noticed by previous authors. In the same plots we also show the results of a fit between M_{dyn} and M_c , obtained on the basis of the setting of the BL. There seems to be little doubt that the latter fit is better. The average values of M_{dyn}/M_c are both $\sim 0.97 \pm 0.03$, quite close to unity and consistent with it at the $1-\sigma$ level.

We have also compared the shapes of the cluster (integral) mass functions $n_c(> M_c)$ and $n_c(> M_v)$. In Fig. 13 and 14, upper and lower plots show their behaviors, respectively. In the same plots, we also show Press & Schechter and Sheth & Tormen theoretical curves. They can be obtained from two different expressions of

$$f(\nu)\nu d \log \nu = \frac{M}{\bar{\rho}_m} n_c(M) M d \log M ; \quad (5.2)$$

here $\bar{\rho}_m$ is matter density, the bias factor $\nu = \delta_c/\sigma_M$ is the ratio of the critical overdensity in the spherical growth model to the rms density fluctuation on the length scale corresponding to the mass M , and $n_c(M)$ is the differential mass function, which shall then be integrated to obtain $n_c(> M)$.

In the Press & Schechter formulation, assuming spherical unperturbed fluctuation growth,

$$f(\nu)\nu = \sqrt{2/\pi} \nu \exp(-\nu^2/2) , \quad (5.3)$$

while Sheth & Tormen, taking into account the ellipsoidal nature of the collapse, argue that

$$f(\nu)\nu = A(1 + \nu'^{-2q})\sqrt{2/\pi} \nu' \exp(-\nu'^2/2) , \quad (5.4)$$

with $\nu' = \sqrt{a}\nu$; this expression introduces the parameters A , q and a , however constrained by the requirement that all matter is bound in objects of some mass M , however small, and therefore the integral of $f(\nu)$ must be unity. In our plots, A is normalized to yield the number of clusters found in simulations, and this constraint is automatically satisfied. Sheth & Tormen (1999) showed that, in the GIF simulations for an SCDM, 0CDM and Λ CDM models (see Kauffmann et al 1999), a good fit to the numerical mass function was obtained if $q = 0.3$, $a = 0.707$.

In Fig. 13 and 14 we report the mass function obtained from eq. (5.4) for these values, for TCDM and Λ CDM, respectively. The fit with the $n_c(> M_v)$ is surely better than using eq. (5.3). We also tried to modify the parameter a , that, according to Sheth & Tormen arguments, is related to the density contrast of virialized structures. As a matter of fact $n_c(> M_c)$ is derived with a variable density contrast, as explained in previous sections, and, however, with an average final density contrast which is $\sim 25\%$ below Δ_v . It is therefore reasonable to expect that a lower value of a is needed to compare theoretical predictions with the numerical behavior of $n_c(> M_c)$. In Fig. 13 and 14, we show the expression (5.4), both for $a = 0.707$ and 0.5. It is also evident that, while $a = 0.707$ provides a good fit for M_v -mass functions, the fit obtained provided by $a = 0.5$ for the M_c -mass function is perhaps better.

The results of these comparisons, altogether, are that: (i) No major variations in the numerical mass function

arises when M_v is replaced by M_c . (ii) Variations however exist, which are of the same order of the differences between the standard theoretical expression (5.3; Press & Schechter) and the improved theoretical expression (5.4; Sheth & Tormen). (iii) When the latter expression is used, the fits to the numerical mass functions are best if different values of the parameter a are used for M_v and M_c (~ 0.7 and 0.5, respectively). The differences between the mass functions $n_c(> M_v)$ and $n_c(> M_c)$ are more evident in the intermediate mass range ($7 \cdot 10^{14} h^{-1} M_\odot < M < 10^{15} h^{-1} M_\odot$). They arise from a widespread “re-shuffling” among the masses of DM halos, when the two definitions are used, causing thereby different numbers of halos in different mass intervals. This can also be seen from Fig. 10, where the mean cluster radii (r_c , r_v) of halos in this mass range show appreciable differences.

6. CONCLUSIONS

Observational work on galaxy clusters made a giant leap forward thanks to X-ray observations and, in turn, cluster data are providing more and more cosmological information. The ROSAT All Sky Survey (RASS) allowed the extraction of large samples of galaxy clusters, like REFLEX (Bohringer et al. 2001) or NORAS (Viana et al. 2001), tracing the large scale structure (LSS) of the Universe up to $\sim 1000 h^{-1}$ Mpc of distance (h is the Hubble constant in units of 100 km/s/Mpc). These data are consistent with the spectrum of a low-density CDM model, with matter density parameter $\Omega_m \simeq 0.3$. Also an analysis of the redshift dependence of the X-ray cluster luminosity function, based on a Press & Schechter approximation, sets a relation between Ω_m and σ_8 , which requires again $\Omega_m < 0.5$, 0.6 (Ω_m : matter density parameter; σ_8 : squared mean density contrast, on the scale of $8 h^{-1}$ Mpc) (Borgani et al. 2001). Such constraints on the model will become more stringent, in the forthcoming years, thanks to XMM-Newton and Chandra data, providing high- z cluster samples with tenths of thousands objects (see, e.g., Bartlett et al. 2001).

In our opinion, such fast improvements of the observational materials deserve to be matched by a suitable effort of the theoretical analysis. In this work we try to contribute to it, by providing an improved pattern to measure individual cluster densities, radii and masses in numerical simulations, without reference to a standard density contrast. Although, both in real samples as well as in simulations, cluster members are directly observable together with their environs, a definition of cluster radii, masses, and density contrasts is needed both for statistical aims, when treating a large set of halos, and for individual objects, e.g., to compare the observed mass distribution with analytical expressions of radial profiles. In the standard approach, a value for the density contrast is usually borrowed from analytical results, which are obtained under assumptions which can be incorrect in the real world, as well as in simulations. Such assumptions, however, were explicitly considered to be the best possible choice. In particular, Cole & Lacey (1996) had explored the possibility to make use of the virial ratio, but considered its value in spheres, instead of layers. Here we see that, passing from the integral to the differential virial ratio $\mathcal{R}(r) = -2T(r)/W(r)$, allows the detection of a neat boundary, where a transition from halo to surrounding material occurs. In fact, first of

all, (i) this inspection allows the detection of minimum points of \mathcal{R} in all halos, which could be easily missed in an integral inspection. Some of them are safely shown not to be numerical features, as they persist without appreciable shifts when we compare different resolution simulations of a given halo. Furthermore, (ii) we found that, CHb quite close to the radius \bar{r} , where one of the persistent minima occurs, there is always a maximum of the function $w(r)$; finally, CHb (iii) at the radius \bar{r} , we have also that

$$w(\bar{r}) \simeq \mathcal{R}(\bar{r}) . \quad (6.1)$$

Let us recall that, in general, $w(r)$ is defined with reference to the behavior of the potential energy around \bar{r} , by setting:

$$W(r) = W(\bar{r})(r/\bar{r})^{-w(r)} \quad (6.2)$$

and, therefore, its r dependence accounts for the radial dependence of $W(r)$.

In this paper we have shown that the above properties (i), (ii), (iii) are consistent with the requirements that: (a) \bar{r} sets a neat boundary between bound and unbound material. (b) A significant interval (depth $\sim 50\text{--}100 h^{-1}\text{kpc}$), where $w(r)$ is constant, lies about \bar{r} . We called it a boundary layer (BL). Accordingly, the r dependence of $W(r)$, inside of the BL, is expressed by eq. (6.1), by replacing the exponent $w(r)$ with its constant value \bar{w} .

The relation between the observed features (i), (ii), (iii) and the properties (a), (b), was shown under the assumption of spherical symmetry. The fact that the conditions (i), (ii), (iii) are not satisfied exactly, but with a (slight) approximation, can be easily attributed to deviations of numerical structures from sphericity. However, such deviations ought to be quite mild, owing to the statistics we performed on a large number of halos, and this indicates that violent relaxation erased most previous a -spherical features. Non-spherical collapses, however, leave a substantial imprint on the final density contrasts Δ_c found for virialized halos whose spread accounts for different initial 3-D geometries of fluctuations and different interactions with the environment during the collapsing stages.

The simulations used to focus the above properties, at different levels of resolution, in ΛCDM and ΛCDM modes, were run both with the GADGET and the ART codes. Results do not depend on the code. We could also extend the analysis, at the lowest resolution level, to simulations run in quite large boxes ($360 h^{-1}$ Mpc aside),

where we had a large statistics of clusters (> 300 with $M_c > 4.2 \cdot 10^{14} h^{-1} M_\odot$, for each model). We applied to all of them an Rw -requirement, meant to detect the BL, and found it in 97% of the clusters considered. *A detailed inspection of these clusters shows that the mass M_c within the BL substantially coincides with the mass M_{dyn} , evaluated from the velocities of all particles within $r_c = \bar{r}$, according to the virial theorem.* Furthermore, a direct inspection of the clusters without a BL, showed they were exceptional structures, mostly due to undergoing major merging, which certainly justified a dynamically unsettled condition and a badly a -spherical geometry. Let us however notice (see Fig. 5) that “standard” a -sphericity of halo structures does not appear to be a serious obstacle to BL detection.

At present, model clusters to fit X-ray data are mostly built using hydro-codes. This allows substantial improvements with respect to initial analyses based on pure Newtonian dynamics. There are, however, some features in the interpretation of both kinds of simulations, which rely on a sound definition of the virialization radius R_c . This radius, whose setting immediately follows from the detection of the BL position, corresponds to a wide spread of density contrasts Δ_c , and, in general, is significantly different from the radius R_v , obtained using a given density contrast Δ_v . Even keeping to models without hydrodynamics, it is clear that using different radii R_c and density contrast Δ_c could lead to different relations between L_X , T_X and M_c . As a consequence the one-to-one correspondence between M_c and T_X could be lost and it would no longer be granted that a mass function and a temperature function are substantially equivalent quantities.

ACKNOWLEDGEMENTS

We thank INAF for allowing us the CPU time to perform the ART simulation C and D at the CINECA consortium (grant cnami44a on the SGI Origin 3800 machine). GADGET simulations of high-resolution clusters have been run on the 16 Linux PC Beowulf cluster at the Osservatorio Astronomico di Torino. Alessandro Gardini is thanked for allowing us to make use of the simulations A and B; we also wish to thank him, Loris Colombo and Giuseppe Tormen for useful discussions during the preparation of this paper.

REFERENCES

- Bartlett J., et al., 2001 “Galaxy Clusters and the High Redshift Universe Observed in X-rays” Proceedings of the XXI Moriond Conference, (preprint astro-ph/0106098)
- Boehringer, H., et al., 2000, ApJS, 129, 435 B
- Borgani, S., et al., 2001, ApJ, 561, 13 B
- Brian, G. & Norman, M., 1998, ApJ, 495, 80
- Carlberg, R.G., et al., 1996, ApJ, 462, 32
- Cole, S. & Lacey, C., 1996, MNRAS, 281, 716
- Couchman, H. M. P., 1991, ApJ, 268, L23
- Doroshkevich, A.G., Kotok, E., Novikov, I., Polyudov, A.N., Shandarin, S.F. & Schectman, S., 1980, MNRAS, 192, 321
- Eke, V.R., Cole, S., & Frenk, C.S., 1996, MNRAS, 282, 263
- Eke, V., Navarro, J. & Frenk, C., 1998, ApJ, 503, 569E
- Gardini, A., Murante, G. & Bonometto, S. A., 1999, ApJ, 524, 510
- Ghigna S., Moore B., Governato F., Lake G., Quinn T. & Stadel J., 2000, ApJ 544, 616
- Girardi M., Borgani S., Giuricin G., Mardirossian F. & Mezzetti M., 1998, ApJ, 506, 45G
- Goldstein H., Poole C. & Safko, 2002, Classical Mechanics, 3rd ed. – Addison Wesley pub.
- Gott, R. & Rees, M. 1975, A&A, 45, 365G
- Governato F., Babul A., Quinn T., Tozzi P., Baugh C.M., Katz N., & Lake G., 1999, MNRAS, 307, 949
- Kauffmann G., Colberg J., Diaferio A. & White S.D.M. 1999, MNRAS, 303, 188
- Klypin A., Kravtsov A., Bullock J. & Primack J., 2001. ApJ 554, 903
- Knebe A., Kravtsov A., Gottlöber S. & Klypin A., 2000 MNRAS, 317, 630
- Kravtsov A., Klypin A. & Khokhlov A., 1997 ApJ, 111, 73 K
- Lacey, C. & Cole, S., 1993, MNRAS, 262, 627
- Lacey, C. & Cole, S., 1994, MNRAS, 271, 676
- Lahav, O., Lilje, P.R., Primack, J.R. & Rees, M., 1991, MNRAS, 282, 263E
- Macciò A. V., Gardini A., Ghigna S. & Bonometto S. A., 2002, ApJ, 564, 1M
- Monaco, P & Murante, G., Physical Review D , 60/10 , id. 103502 , 1999
- Navarro J., Frenk C. & White S.D.M. 1996, ApJ, 462, 563
- Navarro J., Frenk C. & White S.D.M. 1997, ApJ, 490, 493

- Peebles P.J.E., 1980, *The Large Scale Structure of the Universe*, Princeton University Press, Princeton
- Power C., Navarro J., Jenkins A., Frenk C., White S.D.M., Springel V., Stadel J. & Quinn T., 2002, MNRAS (submitted) astro-ph/0201544
- Press W.H. & Schechter P., 1974, *ApJ*, 187, 425
- Sheth R.K., Mo H.J. & Tormen G., 2001 MNRAS, 323 ,1
- Sheth R.K. & Tormen G., 1999 MNRAS, 308, 119
- Sheth R.K. & Tormen G., 2002 MNRAS 329, 61
- Schueker P., Caldwell R.R., Boehringer H., Collins C.A. & Guzzo L., astro-ph/0211480 and A&A (in press)
- Springel V., Yoshida N. & White S.D.M., 2001 *NewA*, 6, 79 S
- Viana P., Nichol R. & Liddle A., 2002, *Apj*, 569L, 75, V
- Zel'dovich, Ya. B., 1970 *A&A*, 5,84

APPENDIX A

Let us assume that halos are spherically symmetric. If BL's are in virial equilibrium, at any r , in their interior

$$\langle v^2 \rangle = -\phi = G \frac{M(< r)}{r}, \quad (\text{A1})$$

$M(< r)$ being the mass inside r . According to kinetic gas theory, however, $p = \rho \langle v^2 \rangle / 3$. Accordingly, local equilibrium prescribes that $p = -\rho \phi / 3$ and, up to first order in $\Delta r / r$,

$$\begin{aligned} 3[p_+ V_+ - p_- V_-] &= \frac{4\pi}{3} G \rho_- r_-^{3-\beta} \left[\frac{M_+}{r_+^{1-\beta}} - \frac{M_-}{r_-^{1-\beta}} \right] \simeq \\ &\simeq 4\pi G \rho_- r_-^3 \frac{2\beta - 1}{3} \frac{M_-}{r_-} \frac{\Delta r}{r_-} \end{aligned} \quad (\text{A2})$$

with a β value such that $\rho r^{3-\beta}$ is constant across Δr (indices \pm indicate that a quantity is evaluated in r_\pm).

Let us compare this term with the potential energy of the layer

$$W = G \int_{r_-}^{r_+} d^3 r \rho(r) \frac{M(< r)}{r} \simeq 4\pi G \rho_- r_-^3 \frac{M_-}{r_-} \frac{\Delta r}{r_-}, \quad (\text{A3})$$

also evaluated assuming spherical symmetry and neglecting terms of higher order in $\Delta r / r$. The ratio between pV terms and potential energy is $\simeq (2\beta - 1)/3$ and would vanish for $\beta = 0.5$.

Let us now assume to be dealing with halos whose profile is $\rho(r) \simeq \rho_o \chi(r/r_s)$ with

$$\chi(x) = [x^\alpha (1 + x)^{3-\alpha}]^{-1}, \quad (\text{A4})$$

where r_s is the scale radius of the profile and the concentration of the halo is $c = r_s / r_v$. This profile is found for most halos in our simulations, up to $r < r_v$, with a value of c in the interval 4–7 and values of $\alpha \simeq 1$; this agrees with previous numerical analyses (see, e.g., Navarro et al. 1996, 1997, Ghigna et al 2000, Klypin et al 2001, Power et al 2002), also extended to smaller values of r , finding values of α ranging between 0.8 and 1.2. Using this profile we can evaluate the r dependence of β for α values in the above interval. Such values are shown in Fig. 15 and indicate that for $c \sim 4$ –7, $\beta \sim 0.5$ –0.3.

This shows that the contribution of the pressure terms to the virial balance is expected to be significantly smaller than the contribution of the potential term.

Let us however add some further comments:

(i) Using the profile in eq. (A4) for $r \gg r_v$ is an approximation. An inspection of numerical halos, already significantly inhomogeneous at such radii (see, e.g., Fig. 5), shows that the slope of the profile is often smoother there.

(ii) Accordingly, owing to eqs. (A2)–(A3), the pV terms can be absorbed in a factor (~ 1), set in front of the potential term of the virial balance. This correction does not cause any displacement of the point where \mathcal{R} has its minima. On the contrary, it may interfere with the condition $w = \mathcal{R}$, which, in principle, can be suitably improved.

(iii) Deviations from spherical symmetry, however, are far from being fully negligible and the discrepancies between \mathcal{R} and w , found in halo analysis, show that a correction of \mathcal{R} by $\sim 10\%$, would not improve the efficiency of the method.

APPENDIX B

We tried to find a BL, i.e. to apply the Rw requirement, also in two N–body simulations aimed at studying the evolution of a galactic stellar disk in a cosmological context. These simulations, performed with GADGET, will be discussed in a forthcoming paper (Murante, Curir & Mazzei, in preparation). Here we used simulations with DM only (no galactic disk is present).

In the first one, initial conditions were set up with the same multi–mass technique described in Sec. 2, using the ART package. A DM halo, whose mass is $M_v = 1.14 \times 10^{11} h^{-1} M_\odot$ at redshift $z = 0$, was simulated at high–resolution using DM particles of mass $M_p = 1.21 \times 10^6 h^{-1} M_\odot$. According to eq. (1.1), the virial radius $r_v \approx 0.125 h^{-1}$ Mpc. External forces were taken into account by setting heavier and heavier particles in 3 concentric shells. We checked that no intruders (heavier mass particles) were ever closer than $0.5 h^{-1}$ Mpc from the center of mass of the halo. The Rw requirement was applied to this halo, at redshifts $z = 0$ and $z = 2$.

At $z = 0$ a BL was found, with a radius $r_c = 0.113 h^{-1}$ Mpc, yielding a ratio $M_c / M_{dyn} = 1.0502$. On the contrary, at $z = 2$, we could not find a good fit for the χ^2 parameter used to implement the Rw requirement. It should be noticed that these results held, in spite of the fact that the halo concentration is $\simeq 20$.

This suggests that BL's are found by the Rw requirement also when the condition $pr^3 = \text{const.}$ is (mildly) violated; on the contrary, no BL is found when the *the halo is not yet virialized*, as it was at $z = 2$ and is also confirmed by direct inspection. Apparently, the presence of a BL however distinguishes gravitationally relaxed objects from those still in an evolutionary phase.

A partial confirm of these two results comes from the application of the Rw requirement to a second simulation, following the evolution of an isolated halo of nominal mass equal to the previous one, with a nominal radius of $R = 0.180$ Mpc, generated with a NFW density profile (see eq. A4) and with initial particle velocities picked up from a multivariate Maxwellian distribution; the NFW density profile was cut off at the nominal radius; the concentration c was set to the value measured in the previous case (using r_v to evaluate it, as in Navarro et al, 1997). The halo was evolved for ≈ 10 Gyr, to reach the age of the Universe at $z = 2$ in a Λ CDM cosmology where $\Omega_\Lambda = 0.7$ and $\Omega_m = 0.3$.

We applied the Rw algorithm, to find a BL at the beginning ($t = 0$ Gyr) and at the end ($t = 10.23$ Gyr) of the simulation. No BL could be found at $t = 0$, when the halo was *not* in equilibrium. Apparently, therefore, the presence of a BL is characteristic of gravitationally stable objects, independently of the geometrical distribution of particles. At $t = 0$, a SO algorithm, based on a purely geometrical prescription, would comfortably detect a halo. The Rw requirement, instead, which is based on dynamical prescriptions, appears to be more selective than purely geometrical recipes.

At $t = 10.23$ Gyr, we find a layer fulfilling the Rw requirement, with $r_c = 0.023$ Mpc, yielding $M_c/M_{dyn} = 1.0201$. This happens in spite of the value of the density contrast at r_c , which is quite large ($\rho/\rho_{crit} = 2457$). In this (quite peculiar) case, the definition of virialization based on the density contrast fails, in spite of the fact that gravitational equilibrium is established.

These arguments seem to indicate that a technique based on the Rw requirement is applicable on a wide range of DM halo masses, even when c is fairly large; mild deviations from the requirement that pr^3 is constant do not seem to destroy its effectiveness. Further analysis will be performed to put precise limits to the cases when the Rw criterion is a useful tool for telling apart virialized halos from still strongly evolving ones.

	TCDM (A)	Λ CDM (B)
Ω_m	1	0.35
Ω_Λ	0	0.65
$\Omega_b \cdot 10^2$	6	3.6
n	0.8	1.05
h	0.5	0.65
σ_8	0.55	1.08
Γ	0.32	0.19

TABLE 1
PARAMETERS FOR THE SIMULATIONS PERFORMED BY THE AP3M CODE.

	TCDM (C)	Λ CDM (D)
Ω_m	1	0.3
Ω_Λ	0	0.7
$\Omega_b \cdot 10^2$	5	2.6
n	0.8	1.05
h	0.5	0.7
σ_8	0.55	1.08
Γ	0.31	0.21

TABLE 2
COSMOLOGICAL PARAMETERS FOR THE ART SIMULATIONS.

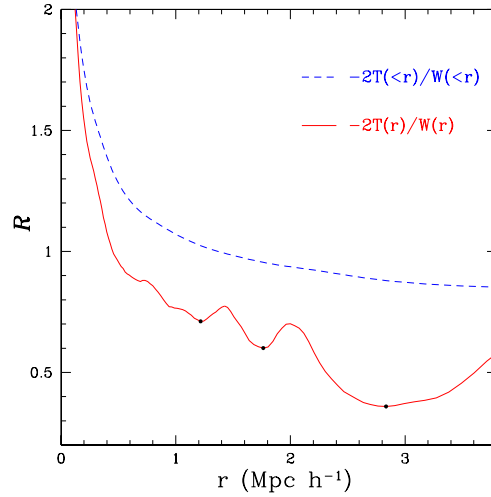


FIG. 1.— Integral (dashed line) and differential (solid line) virial ratios $\mathcal{R}(> r)$ and $\mathcal{R}(r)$ are plotted against the halo radius r for a Λ CDM halo. Heavy dots indicate the points where the differential \mathcal{R} has minima.

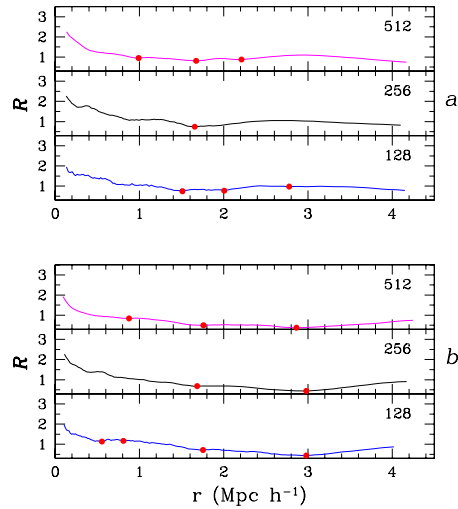


FIG. 2.— The virial ratio $\mathcal{R} = -2T/W$ is plotted against the halo radius r , at different resolution levels. The value of N shown in each box yields the number N^3 of particles used at the highest resolution level. Heavy dots show the setting of the *permanent* minima. The plots (a) and (b) refer to Λ CDM and TCDM clusters, respectively. The minima fulfilling the Rw requirement lay at $\sim 1.62 h^{-1} \text{Mpc}$ and at $\sim 1.75 h^{-1} \text{Mpc}$ for the halos *a* and *b*, respectively.

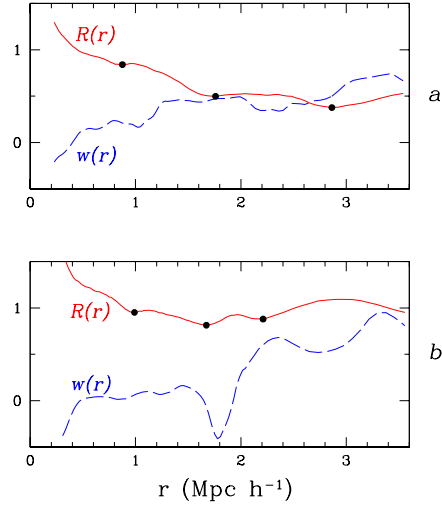


FIG. 3.— The \mathcal{R} and w dependence on r is shown in the best and worst cases treated at the highest resolution level, (*a* and *b*, respectively); still at this resolution, the w behavior is rather noisy (compare however with Fig. 4, to see how better resolution reduces numerical noise). According to the Rw requirement, the case *a* shows a neat intersection of the two curves for a maximum of w and a minimum of \mathcal{R} . However, also in the case *b*, the correspondence between the maximum of w and the minimum of \mathcal{R} is apparent.

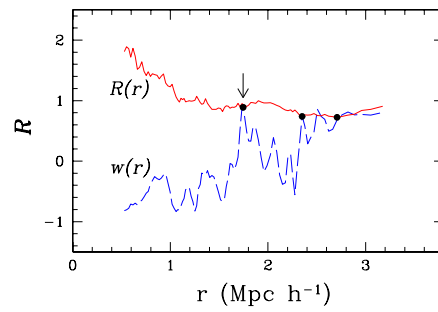


FIG. 4.— A typical example of \mathcal{R} and w behaviors at the initial resolution level. This halo is the same shown in Fig. 3*a*, at higher resolution.

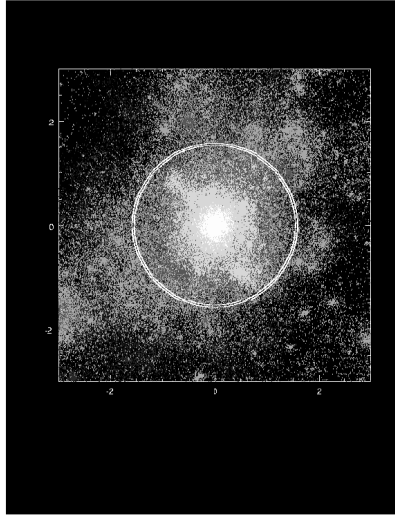


FIG. 5.— Image of a typical cluster, with the location of the boundary layer (BL). The cluster shown has a radius $r_c = 1.76 h^{-1} \text{Mpc}$, a mass $M_c = 8.92 \cdot 10^{14} h^{-1} M_\odot$ and a density contrast $\Delta_c = 141$. The m.s. velocity of particles within r_c is 1574 km/s. This cluster is taken from simulation D. Gray scales refer to particle velocities.

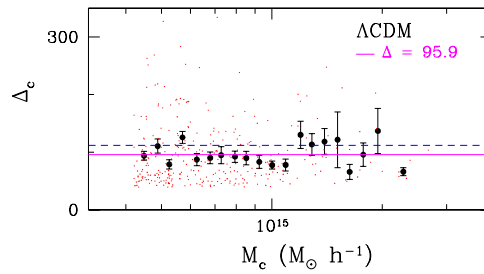


FIG. 6.— The mass dependence of the density contrast is shown. Points refer to all clusters in the simulation B (Λ CDM). Heavy points give the average Δ_c for each M_c interval (constant logarithmic width). Bars are $1\text{-}\sigma$ errors of the averages. The thick horizontal line is the average value of Δ_c . The dashed line is the virial density contrast Δ_v expected for an unperturbed spherical fluctuation growth.

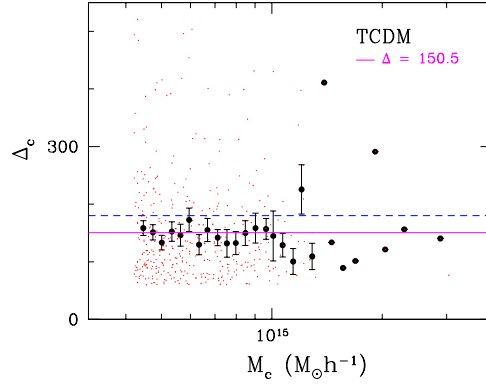


FIG. 7.— The same as Fig. 6 for clusters in simulation A (TCDM). At high M_c some heavy points are shown without error bars, when there is one cluster per logarithmic mass interval.

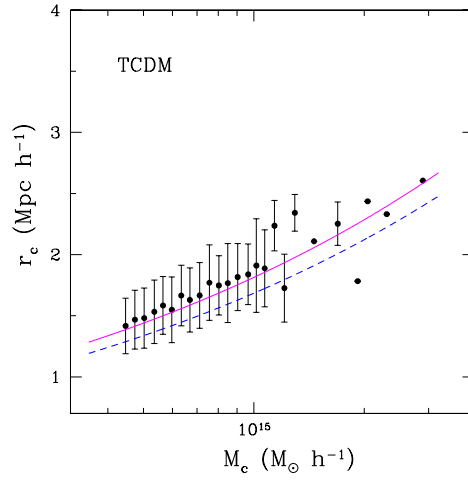


FIG. 8.— Average cluster radii (heavy dots) are plotted against their masses M_c for the simulation A. The solid line is obtained for the average density contrast (150.5); the dashed line, instead, is obtained from the “virial” density contrast (178). Error bars yield the variance of cluster radii around their averages.

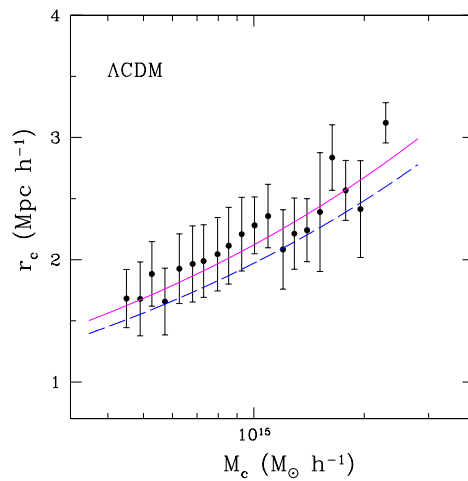


FIG. 9.— The same as Fig. 8, for the simulation B. Solid and dashed lines correspond to density contrasts 95.9 and 111, respectively.

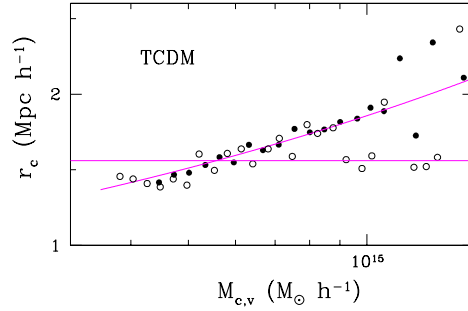


FIG. 10.— We show how “virial” quantities can introduce spurious characteristic scales, if fit against “real” quantities. Here mean cluster radii (r_c) are plotted against M_c (filled circles) and M_v (empty circles). Error bars are omitted to avoid confusion (see, however, Fig. 7). The horizontal line could be interpreted as a mass-independent average radius for all clusters.

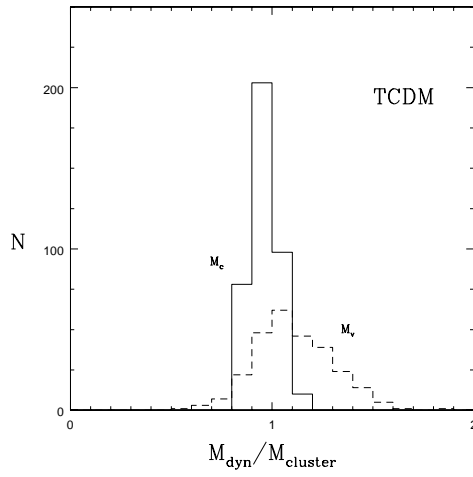


FIG. 11.— The ratio between masses evaluated from particle velocities, according to the virial theorem (M_{dyn}), and summing particle masses ($M_{cluster}$) is shown limiting clusters either at r_c or at r_v , for all clusters of simulation A.

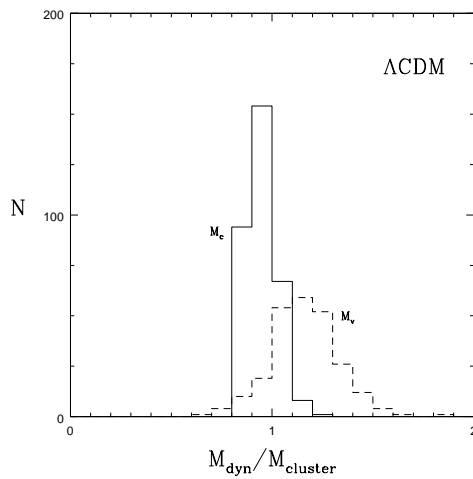


FIG. 12.— The same as Fig. 11 for simulation B.

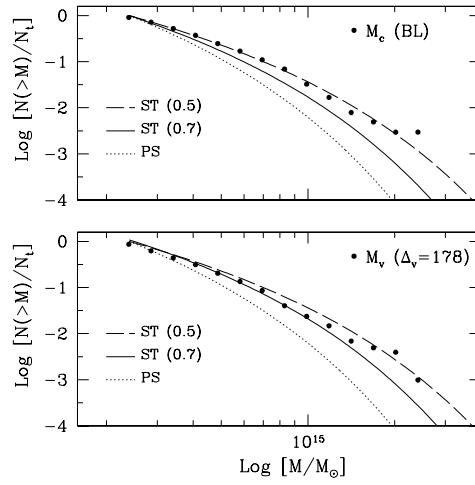


FIG. 13.— Comparison between mass functions obtained using BL or virial quantities (TCDM).

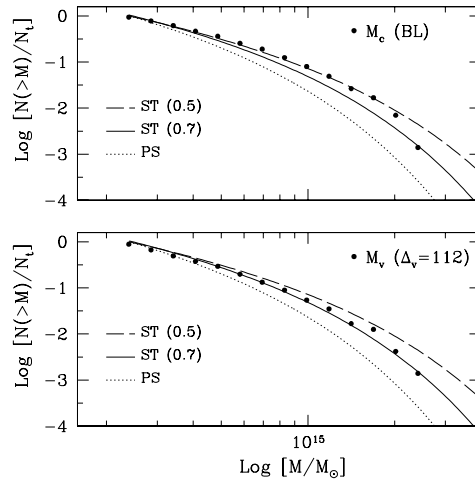


FIG. 14.— Comparison between mass functions obtained using BL or virial quantities (Λ CDM).

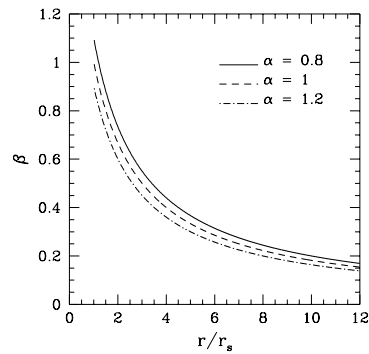


FIG. 15.— β yields the deviation from 3 of the slope of the halo profile in the region where the BL is expected to lay.